PCCP

ROYAL SOCIETY OF CHEMISTRY

PAPER

View Article Online
View Journal | View Issue

Cite this: *Phys. Chem. Chem. Phys.*, 2021, **23**, 10509

The formation and evolution of carbonate species in CO oxidation over mono-dispersed Fe on graphene

Jiang Zhu,*[a] Xining Feng,[a] Xin Liu,*[b] Xin Zhang,[b] Yong Wu,[b] Hongdan Zhu,[b] Yang Yang,[b] Ting Duan,[b] Yanhui Sui,[b] Yu Han*[c] and Changgong Meng*[b]

Fe is not only the most abundant metal on the planet but is also the key component of many enzymes in organisms that are capable of catalyzing many chemical conversions. Mono-dispersed Fe atoms on carbonaceous materials are single atom catalysts (SACs) that function like enzymes. To take advantage of the outstanding catalytic performance of Fe-based SACs, we extended a CO oxidation reaction network over mono-dispersed Fe atoms on graphene (FeGR) by first-principles based calculations. FeGR-catalyzed CO oxidation is initiated with a revised Langmuir–Hinshelwood pathway through a CO-assisted scission of the O–O bond in peroxide species (OCOO). We showed that carbonate species (CO_3), which were previously generally considered as a persistent species blocking reaction sites, may form from CO_2 and negatively charged O species. This pathway competes with desorption of CO_2 and reduction of the Fe center with gaseous CO, and it is exothermic and inevitable, especially at low temperatures and with high CO_2 content. Although direct dissociation of CO_3 is demanding on FeGR, further adsorption of CO on Fe in CO_3 is plausible and takes place spontaneously. We then showed that adsorbed CO may react with CO_3, forming a cyclic-carbonate-like species that dissociates easily to CO_2. These findings highlight the reaction condition-dependent formation and evolution of CO_3 as well as its contribution to CO conversion, and it may extend the understanding of the performance of SACs in low temperature CO oxidation.

Received 22nd February 2021,
Accepted 6th April 2021

DOI: 10.1039/d1cp00814e

rsc.li/pccp

1. Introduction

Fe is not only the most abundant transition metal on the planet but is also the key component of the reaction centers of many enzymes in organisms, such as cytochrome P450,[1,2] nitrogenase,[3] and methane monooxygenase,[4] as well as in many Fe complexes,[5–7] which are found to be catalytically efficient in many industrially important chemical processes, including the selective oxidation of hydrocarbons.[8,9] Recently, considerable attention has been continuously paid to the controlled synthesis and application of heterogeneous transition metal SACs that inherit not only the merits of enzymes and metal complexes with each mono-dispersed transition metal atom as a reaction center for efficient chemical conversion, but also the advantages of heterogeneous catalysts for the reusability of the catalyst and easy product separation.[10–16] Many graphene-derived SACs of Fe,[8,9,17–28] Ni,[29] Co,[18] Mn,[30] Pd,[31–36] Au,[37–40] Pt,[41–43] Ru,[44] *etc.*, have been investigated and were proposed to be efficient in many processes of industrial significance.[45] Fe-Based SACs on graphene and graphene-related materials were shown to be effective for the oxidation of arenes,[8] oxygen reduction,[9,17–20] the nonoxidative conversion of methane to ethylene and aromatics,[26] water oxidation,[18] the elimination of formaldehyde,[21,22] CO oxidation,[23,24,27,28] the oxidative conversion of methane,[25] *etc.* In Fe-based SACs, enzymes and complexes catalyzed chemical conversion, and the robust and reversible coordination of the reaction species effectively stabilized Fe as reaction centers in mono-dispersed form and maintained efficiency of the conversion. The dominant role of the electronic structure in the performance of a specific catalyst has been well recognized.[34,45,46] Considering the mono-dispersed under-coordinated nature of metals in SACs and the dynamic adsorption and conversion of substrates in reaction conditions, the impact of reaction species on metal centers would be more pronounced, and it may stabilize or even drive further evolution of metal centers, switch the reaction mechanisms and contribute to the conversion and product selectivity.[47–51]

[a] *School of Chemistry and Chemical Engineering, Liaoning Normal University, Dalian, 116029, P. R. China. E-mail: zjryan@lnnu.edu.cn*
[b] *State Key Laboratory of Fine Chemicals, Department of Chemistry, Dalian University of Technology, Dalian, 116024, P. R. China. E-mail: xliu@dlut.edu.cn, cgmeng@dlut.edu.cn*
[c] *KAUST Catalysis Center (KCC), King Abdullah University of Science and Technology, Thuwal 23955-6900, Saudi Arabia. E-mail: yu.han@kaust.edu.sa*

To this end, mechanism investigations on SAC-catalyzed chemical conversion in conditions relevant to experiments would be more helpful to rationalize the understanding of the observed superior performance of SACs.[34,45]

CO oxidation is one of the most investigated heterogeneous reactions. Due to the strong affinity of conventional transition metals to CO, O_2 activation and dissociation in CO oxidation conditions are demanding.[52] Combining experimental and theoretical efforts, people showed that CO oxidation may take place through a revised Langmuir–Hinshelwood pathway, an Eley–Rideal pathway or their variants over SACs supported on non-reducible supports. Eley–Rideal-type pathways can be identified by the direct reaction of O_2 or CO, either in gas phase or from the van de Waals complexes, as surface species for formation of CO_2[53] or various transition metal carbonates in form of CO_3,[23] OCOOCO,[54] *etc.* In revised Langmuir–Hinshelwood type pathways, O_2 dissociation is facilitated by coadsorbed CO, and the reaction involves peroxide species.[40,42,52,55] CO_3 species has long been considered as an ultrastable species blocking reaction sites in CO oxidation, and it has been widely used in discussions on mechanisms of reactions involving CO and the catalytic performance of SACs.[56] It was also recently proposed to contribute to CO conversion over Pt/Al_2O_3.[57,58] However, the formation, evolution and role of CO_3 in CO oxidation reaction conditions over SACs have not been well discussed before. In this work, we extended the reaction network for CO oxidation over FeGR with consideration of the reaction condition-dependent formation and evolution of CO_3 species, *etc.*, which may be one of the origins of the superior catalytic performance of SACs at low temperatures. These findings would help to rationalize the current understanding of the impact of the reaction conditions on the catalytic performance of SACs.

2. Theoretical methods

All the results were obtained with the Perdew–Burke–Ernzerhof functional and DSPP pseudopotential as implemented in DMol^3.[59–64] The electronic structures and reaction mechanisms on FeGR were investigated with a (6 × 6) supercell of graphene with an Fe/C ratio of 1 : 71. The reported structures were fully relaxed without any constraints. Transition states (TSs) were located through linear and quadric synchronous transit methods. Frequency calculations were performed for all the reported structures. The TSs were further optimized and confirmed with the only imaginary frequency in the reaction direction.[65,66] We used a 4 × 4 × 1 *k*-point grid for the structure optimization and TS search as well as for the frequency calculations. Hirshfeld charges were used for population analysis.[67] The formation free energies of potential reaction species were calculated from first-principles data with statistical mechanics methods at $P_{CO}:P_{O_2}$ = 1 : 20, P_{CO} = 0.01 atm at 298 K with respect to single-vacancy graphene, Fe atom, gaseous CO, O_2 and CO_2. ΔE_r and ΔG_r were used to describe the energy and free energy barriers of the elementary steps and were calculated as the difference in the electronic energy and free energy between the reactants and transition states, respectively. The calculated lattice parameters of bulk body-centered-cubic Fe and graphene are 2.74 and 2.46 Å, respectively.[68,69] The formation energy and binding energy of Fe atom of a single-vacancy defect on graphene were calculated as 7.74 and −7.52 eV, respectively.[22,23,70–72]

3. Results and discussion

3.1 Potential reaction species on FeGR

We firstly investigated the stability of potential reaction species formed over FeGR (Fig. 1). The binding of an Fe atom to defective graphene (FeGR, Fig. 1a, E_b = −7.52 eV) is 7 eV more exothermic than that on pristine graphene (E_b = −0.46 eV).[23] In FeGR, Fe is 0.27 |*e*| positively charged, and the Fe–C distances are 1.78 Å; these findings are in reasonable agreement with the recent observation of positively charged mono-dispersed Fe species on graphene and N-doped graphene.[9,23,25] O_2 is activated upon adsorption, and it lies right above and coordinates with Fe at the corner of a distorted tetrahedral formed together with 3 interfacial C atoms at Fe–O and O–O distances of 1.88, 1.91 and 1.38 Å, respectively (Fig. 1b, E_{ad} = −1.81 eV). CO binds FeGR in the reverse direction to one interfacial Fe–C bond at Fe–C(CO) and C–O distances of 1.86 and 1.16 Å, respectively (Fig. 1c, E_{ad} = −1.48 eV). CO adsorption on Fe with the C–O bond vertical to the graphene plane was found to be 0.02 eV less plausible. Coadsorption of CO and O_2 may occur (Fig. 1d), and the calculated E_{ad} is −2.19 eV. In this structure, the O–O (O_2) and C–O (CO) distances are 1.33 and 1.15 Å, respectively, slightly shorter than those in mono-molecular adsorption (Fig. 1b and c). The coadsorption of 2CO was also investigated (2CO, Fig. 1e, E_{ad} = −2.64 eV). Similar to the case of CO, the 2CO also bind Fe in the reverse direction to the interfacial Fe–C bonds at Fe–C(CO) and C–O distances of 1.83 and 1.16 Å, respectively. As for the coadsorption of $2O_2$ ($2O_2$, Fig. 1f, E_{ad} = −1.64 eV), the

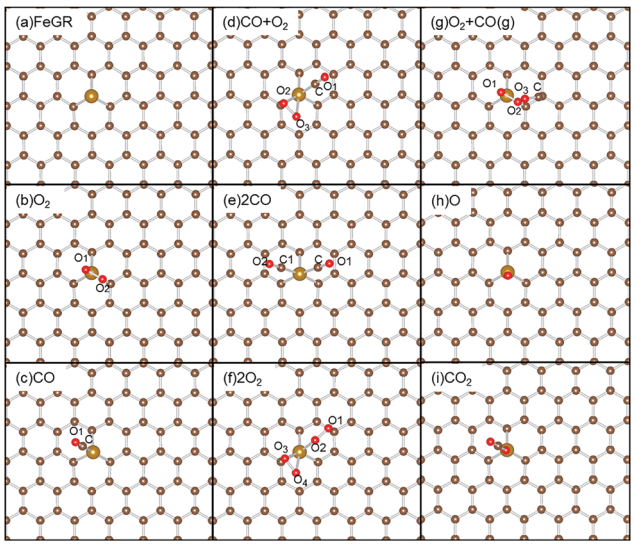

Fig. 1 Top views of the optimized atomic structures of the potential reaction species on FeGR under CO oxidation conditions. Fe, C, and O are shown in gold, brown and red, respectively.

orientations of the $2O_2$ with respect to the Fe center are similar to those in CO + O_2, except that an O_2 takes the place of CO. The stability of the van der Waals complex of preadsorbed O_2 and gaseous CO (CO + O_2(g), Fig. 1g, E_{ad} = −1.84 eV) was found to be similar to that of O_2 (E_{ad} = −1.81 eV). O atomic adsorption is generally considered to be an important reaction intermediate from the dissociation of peroxide or carbonate species on revised Langmuir–Hinshelwood or Eley–Rideal pathways for CO oxidation and was found to be plausible with O standing 1.62 Å on top of the Fe center (O, Fig. 1h, E_{ad} = −4.90 eV).[23,40] CO_2 adsorption (CO_2, Fig. 1i, E_{ad} = −0.41 eV) with one O(CO_2) 2.10 Å above the Fe center and a C–O–Fe angle of 149° is plausible. The E_{ad} of O_2 is more significant than that of CO; O_2 adsorption would be dominant under the conventional conditions for characterization of CO oxidation performance with $P_{O_2}:P_{CO}$ at the level of at least 10.[73] Because the stabilities of O_2 + CO(g), $2O_2$ and 2CO (Fig. 1e–g) are only comparable to or even less than that of O_2 or their formation may involve desorption of O_2, their populations would be quite limited on FeGR in O_2 lean CO oxidation conditions, and they were not considered.

The stretching frequencies of CO in these surface species were also calculated. For freestanding CO, the calculated frequency is 2083 cm^{-1}. This frequency shifted to 1978 and 2007 cm^{-1}, respectively, after adsorption (CO, Fig. 1c) and in CO + O_2 (Fig. 1d), and it further shifted to 1999 cm^{-1} in 2CO (Fig. 1e), indicating charge transfer among FeGR and the adsorbates. The stretching frequency of axial CO in $Fe(CO)_5$ in D_{3h} symmetry was reproduced as 2003 cm^{-1} and agrees well with the experimental observation of 2014 cm^{-1}.[74] These calculated CO stretching frequencies are not only consistent with the positively charged nature of the mono-dispersed Fe atoms, but also provide direct evidence for the reliability of the current theoretical approach for investigation of CO oxidation over FeGR.[75–77]

3.2 Conventional revised Langmuir–Hinshelwood pathway

We then investigated the potential pathways for CO oxidation on FeGR. O_2 dissociation on FeGR was investigated firstly to check whether reactive oxygen species can be formed prior to CO adsorption. Although O_2 gains charge from FeGR and is activated, according to the extension of the O–O bond to 1.38 Å, there is still a significant reaction barrier (ΔE_r) of ∼2.00 eV for O_2 dissociation. This barrier can be attributed to the poor stability of O atom originating from the limited binding sites on FeGR. This barrier is already more significant than the calculated E_{ad} of O_2 (−1.81 eV); therefore, O_2 may desorb prior to dissociation.[34,39,78] As O_2 adsorption is more plausible than CO adsorption, Eley–Rideal-type pathways can only be initiated with the reaction between gaseous CO or CO in van der Waals complexes formed between CO and preadsorbed O_2.[23] According to the symmetry of the molecular states of gaseous CO and O_2, only the interactions between 5σ of CO gaseous with the π* states of O_2 in the direction with O(O_2)–C–O of ∼120° is allowed, and the reaction may lead to direct formation of CO_2.[53] However, a close examination of the structures of the expected van der Waals complexes and that for CO + O_2 coadsorption shows that the latter (Fig. 1d) is in fact a global minimum on the potential energy surface of gaseous CO and preadsorbed O_2, and Fe would interact with CO to achieve a plausible octahedral coordination environment. In this sense, the population of CO + O_2 species (Fig. 1d) would be significantly higher than that of O_2 + CO(g) (Fig. 1g). Furthermore, gaseous CO is not activated, and its direct reaction for CO_2 formation may experience a reaction barrier comparable to that for O_2 dissociation on FeGR. Reaction barriers reported for CO oxidation on Pt/4N–graphene (1.81 eV), Fe (1.18 eV) and Cu-doped h-BN (1.91 eV) through Eley–Rideal-type pathways[79–81] are in line with the current proposal. These findings not only explain the difference in stability between CO + O_2 and O_2 + CO(g), but also suggest that CO oxidation initiates from the coadsorption of CO + O_2 with a revised Langmuir–Hinshelwood pathway with the CO-facilitated scission of the O–O bond on FeGR (Fig. 2).

The ΔG value for coadsorption of CO with O_2 (LH-IS1, Fig. 2b) is 0.27 eV higher than that of O_2/FeGR (Fig. 2m), showing that LH-IS1 would be reactive but with a lower population in O_2-lean conditions.[82] In LH-IS1, O(O_2) and C(CO) are −0.08 and 0.13 $|e|$ charged, respectively, and the electrostatic interaction drives them to move to and interact with each other. The transition state (LH-TS1) connecting to a peroxide species (LH-MS1) is reached when the O–C distance decreases to 1.72 Å. The calculated ΔE_r and ΔG_r for the reaction to LH-MS1 are 0.62 and 0.60 eV, respectively. LH-MS1 is a typical peroxide according to the O–O distance (1.56 Å) and O–O stretching frequency (717 cm^{-1}).[83] The calculated CO stretching frequency of LH-MS1 is 1743 cm^{-1}, and this is in reasonable agreement with experiments.[58,78,84] LH-MS1 then undergoes dissociation by passing a transition state (LH-TS2) corresponding to scission of the O–O and C–Fe bonds to form CO_2 (LH-FS1). In this process, the C═O distance remains 1.21 Å, while the O–O and Fe–C distances are stretched to 1.72 and 2.18 Å, respectively. The Hirshfeld charges on the C and 2O(O_2) atoms are 0.14, −0.14 and −0.08 $|e|$, respectively, in LH-TS2 and are 0.28, −0.14, −0.29 $|e|$, respectively, in LH-FS1, indicating that Fe is oxidized in this process. At 298 K, P_{CO} = 0.01 atm and P_{CO}/P_{O_2} = 1 : 20, ΔG for CO_2 desorption is only 0.10 eV; therefore, the formation of the bare O adsorption structure (LH-FS1a, Fig. 2g) would be highly reversible. There is also a strong dependence of the ΔG value for CO_2 desorption on P_{CO_2} and temperature (Fig. 2m, insets). CO_2 desorption is nearly thermo-neutral and is only favored at high temperature and low P_{CO_2}.

According to the conventional revised Langmuir–Hinshelwood pathway for CO oxidation over SACs, the subsequent reaction may take place between gaseous CO and O(Fe). A van der Waals complex (LH-IS2, Fig. 2h) that is endothermic with respect to LH-FS1a is formed firstly. The reaction starts with charge transfer between the highest energy occupied orbital of CO with σ symmetry to the O(Fe) states of π* symmetry. Driven by electrostatic interaction, CO moves in the direction of O(Fe) and reaches the transition state (LH-TS3, Fig. 2i), in which C–O(Fe) is decreased to 1.87 Å. Another CO_2 adsorbed on FeGR (LH-FS2, Fig. 2j) is formed after passing LH-TS3, where ΔE_r is 0.34 eV (ΔG_r is 0.33 eV at 298 K). Considering the weak binding of CO_2 (E_{ad} = −0.41 eV), further desorption of CO_2 would be facile with coadsorption of other gaseous species, even at room temperature.

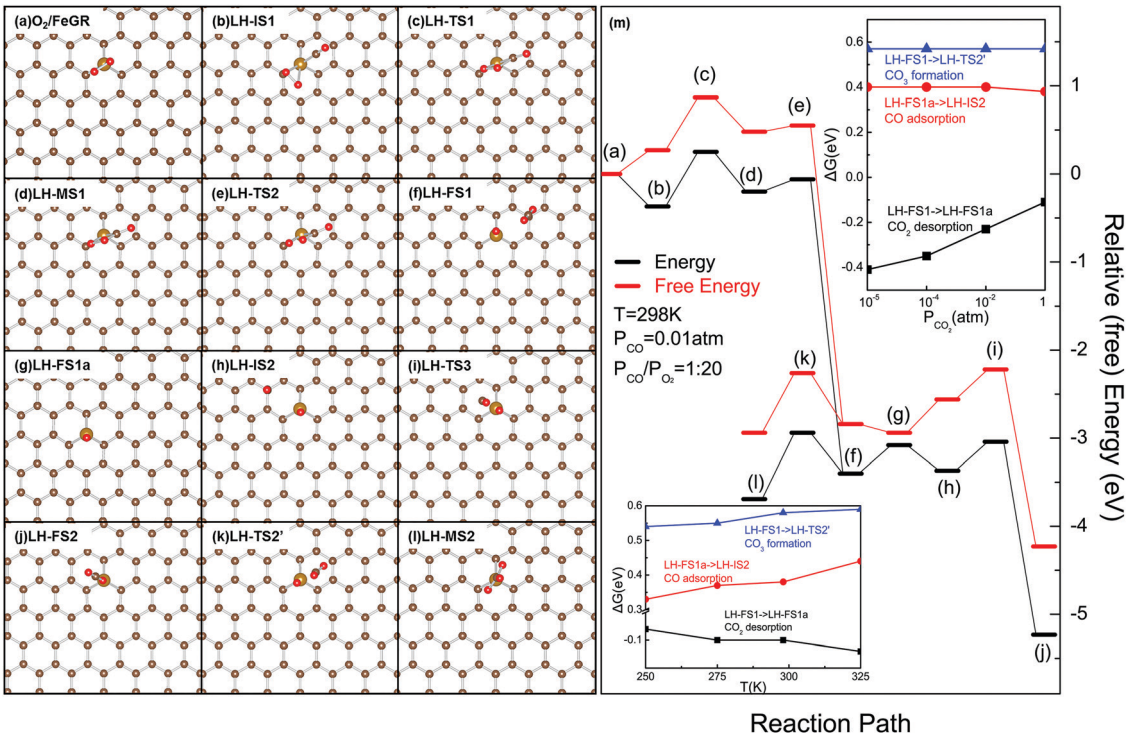

Fig. 2 Atomic structures of potential reaction species (a–l) in CO oxidation over FeGR through the conventional revised Langmuir–Hinshelwood pathway and the corresponding (free) energy profiles with respect to the O_2 adsorption structure (m). The ΔG values for CO_2 desorption and CO adsorption and the ΔG_r values for CO_3 formation were plotted against P_{CO2} (upper inset in m) and temperature (lower inset in m). In (a–l), the C, O and Fe atoms are shown in brown, red and gold, respectively. In (m), species are marked with bracketed letters, as shown in (a–l). All (free) energies were calculated by taking those of O_2/FeGR (a) as zero.

We focused the investigation on FeGR with the Fe–C3 interfacial structure. The calculated formation energies of the single (C3) and double vacancy (C4) defects are 7.74 and 7.83 eV, respectively,[85] while the calculated E_b values of Fe with the Fe–C3 and Fe–C4 interface structures are −7.52 and −6.69 eV, respectively;[86] this suggests that FeGR is thermodynamically more favorable than Fe–C4 and may exist in a large population in SACs synthesized by thermo-driven routes such as pyrolysis. The calculated E_{ad} values of O_2 on Fe–C3 and Fe–C4 are −1.81 and −1.74 eV, respectively, while those of CO are −1.48 and −1.65 eV, respectively.[87] Considering the limited activation of O_2 on Fe–C4 and the high reactivity for weakly bind CO to assist the activation of O_2, the proposed results on FeGR would be more relevant to the experimental findings.

3.3 Formation and evolution of carbonate

It is interesting to note that O in LH-FS1a (Fig. 1g) formed by CO_2 desorption from LH-FS1 is −0.29 $|e|$ negatively charged. Previously, similar negatively charged on-framework and off-framework species in porous materials for CO_2 capture, such as mesoporous activated carbon, metal organic frameworks, and zeolites, were proposed as binding sites.[88] In LH-FS1, the charge transfer from O (Fe═O) to C(CO_2) leads to activation and bending of CO_2, charging one O negatively to interact with the positively charged Fe center. After crossing a transition state (LH-TS2′, Fig. 2k) with ΔE_r of 0.46 eV (ΔG_r of 0.58 eV at 298 K), where the O–C–O angle in CO_2 was distorted to 150.7° and the O(Fe)–C and O(CO_2)–Fe distances were changed to 1.84 and 2.58 Å, respectively, a CO_3 intermediate (LH-MS2, Fig. 2l) was formed. LH-MS2 is 0.29 eV (ΔG = 0.10 eV) more plausible with respect to LH-FS1. In this sense, the formation of CO_3 is inevitable in CO oxidation on FeGR, especially in CO_2-rich conditions and at low temperatures (Fig. 2m, insets). In fact, the formation of negatively charged surface O species (NCSOS) is quite common in CO oxidation. CO_3 was reported even on SACs supported on transition metal oxides, including Pt_1/Fe_3O_4, where CO oxidation is reported to go through Mars–van-Krevelen pathways with the involvement of surface lattice oxygen.[89] On that pathway, the regeneration of surface lattice oxygen with gaseous O_2 may also lead to formation of NCSOS. We proposed that these NCSOSs account for the formation of surface carbonate species. Formation of CO_3 was also reported on transition metal oxides, such as RuO_2, that are highly reactive for CO oxidation.[90] Therefore, the proposed mechanism for CO_3 formation is rather general and relevant to previous experimental findings on various SACs as well as for supported transition metal nanoparticles and oxides.

The evolution of carbonate species was further investigated (Fig. 3). The direct thermo-driven dissociation of carbonate (LH-MS2, Fig. 3a) can be considered as the reverse reaction to the formation reaction (LH-FS1 → LH-MS2, Fig. 2). As LH-MS2 is more plausible than the van der Waals complex formed by CO_2 and the remnant O (LH-FS1), the dissociation of LH-MS2 to LH-FS1 may experience a rather high ΔE_r of 0.75 eV and a ΔG_r

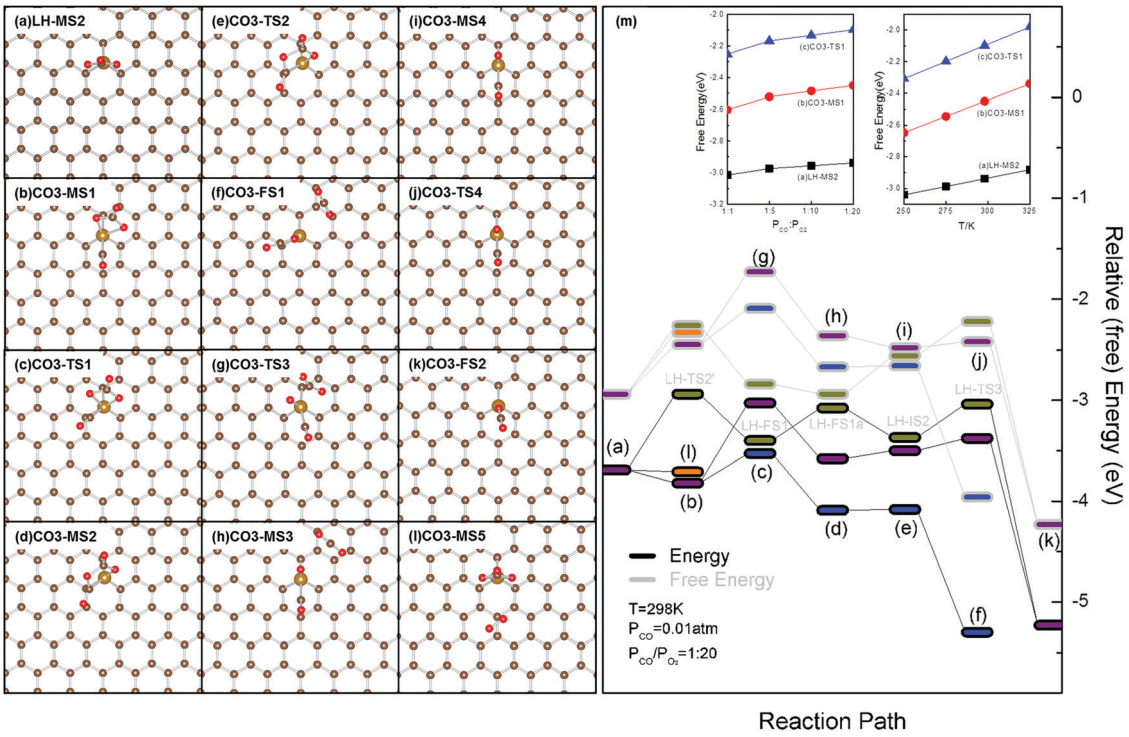

Fig. 3 Potential reaction species (a–l) on pathways for the evolution of CO_3 species and the corresponding (free) energy profiles (m). The C, Fe and O atoms are shown in brown, gold and red, respectively, in (a–l). The species (a–l) were noted with bracketed letters in (m), and their (free) energies were calculated by taking those of O_2/FeGR (Fig. 2a) as zero. In (m), the (free) energies of the reaction species along potential reaction pathways, namely thermo-driven dissociation, evolution with CO present, evolution with CO as an ancillary ligand, and coadsorption of O_2, are shown in dark yellow, blue, purple, and orange, respectively.

of 0.68 eV.[23] Therefore, thermo-driven dissociation of carbonate would be demanding. Furthermore, considering that the desorption of CO_2 would be in equilibrium with the adsorption, while the van der Waals complex of CO (LH-IS2) is also not as plausible as LH-FS1a, the subsequent reactions along the conventional revised Langmuir–Hinshelwood pathway would be highly dependent on the reaction conditions and would be constrained at low temperatures or with high P_{CO_2} (Fig. 2 and 3).

In LH-MS2, Fe was not fully coordinated with 3 interfacial C and 2O of CO_3 in a distorted polyhedral. Further interaction with reaction species, such as CO or O_2, would be possible in the reverse direction to the interfacial Fe–C bond and nearly vertical to the distorted planar CO_3 structure (CO3-MS1, Fig. 3b). The calculated E_{ad} of CO on LH-MS2 is −0.13 eV and ΔG is 0.49 eV at 298 K when P_{CO} is 0.01 atm, suggesting high activity of the adsorbed CO.[34,82] In CO3-MS1, the C═O bond extends to 1.15 Å and the C═O stretching frequency shifts to 2030 cm^{-1}, showing the considerable activation of CO. This is in good agreement with the charge density redistribution between CO and Fe and the significant downshift of the CO molecular states from the Fermi level on the DOS (Fig. 4a, middle and right panel). Specifically, the DOS peaks of the CO 5σ state are even downshifted to right above those of CO 1π. Resonance of the CO states with the O states is also observable in the energy range from −8.0 to −4.0 eV (Fig. 4a, right panel). As for the CO_3 moiety, it binds Fe through 2O that are −0.21 and −0.19 $|e|$ charged at distances of 2.00 and 2.12 Å, respectively. The differences in electronic structure between LH-MS2 and CO3-MS1 suggest that the interaction between CO and O(Fe) is already initiated upon CO adsorption.

Driven by the electrostatic interactions, CO moves to react with O(Fe). In the corresponding transition state (CO3-TS1, Fig. 3c and 4b), the C–O distance in CO remains at 1.16 Å, but the O(Fe)–C(CO) distance decreases from 2.76 to 2.08 Å; meanwhile, the O–C(CO)–O(Fe) angle also decreases from 132° to 117°, showing the tendency for formation of C(CO)–O(Fe) bond and variation of the hybridization state on C(CO) (Fig. 3c and 4b). Accompanying the structure change, the charge transfers among the CO, Fe, O(Fe) and CO_3 moieties are significant (Fig. 4b, middle panel). The Fe, CO and O states are obviously downshifted to achieve better matching in energy (Fig. 4b, right panel), indicating that the C(CO)–O(Fe) interactions are maturing. Specifically, the DOS peaks of the CO molecular states originating from the CO 1π and 5σ states in the range from −8.0 to −5.0 eV are downshifted by ∼1 eV and further split into 5 peaks to resonate with both the Fe-d and O(Fe) states (Fig. 4b, right panel). The calculated ΔE_r and ΔG_r values at 298 K are 0.29 and 0.36 eV, respectively.

In the exothermic process from CO3-TS1, the C(CO)–O(Fe) interaction was further strengthened at the expense of weakening of the C–O and O–Fe interactions, as evidenced by the decrease of the C(CO)–O(Fe) distance to 1.36 Å and the elongation of the C–O and Fe–O distances to 1.48 and 2.73 Å, respectively. It should be noted that one of the O–Fe bonds is

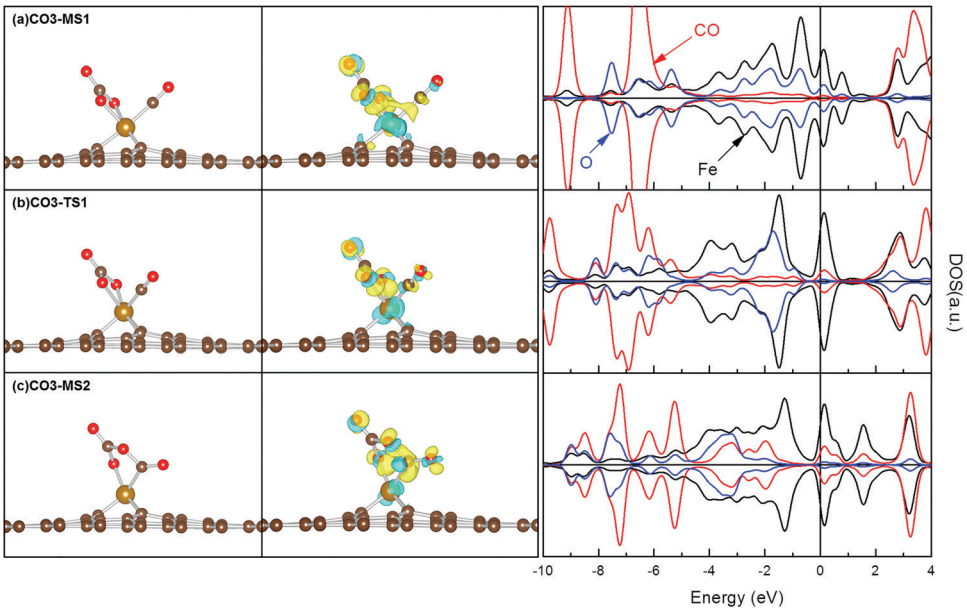

Fig. 4 Structures (left panel), isosurface plots of charge density difference (middle panel) and densities of states (DOS) of the reactant (CO3-MS1, a), transition state (CO3-TS1, b) and intermediate (CO3-MS2, c) on the pathway for evolution of CO_3 species. C, Fe and O atoms are shown in brown, gold and red, respectively. The charge accumulation and depletion regions are shown in yellow and light blue, respectively, and the isosurface values are $\pm 1.0 \times 10^{-6}$ a.u. In the right panel, the DOS curves of Fe, CO and O(Fe) are plotted in black, red and blue, respectively.

activated and attached to C(CO), and CO is thus inserted into the CO_3 moiety, forming quasi-planar C_2O_4 interacting with the Fe center (CO3-MS2, Fig. 3d and 4c). Charge transfer among Fe, the CO_3 moiety and CO is also apparent, confirming the variation of the hybridization state on C(CO) accompanying the structure reorganization after CO3-TS1 (Fig. 4c, middle panel). The DOS peaks of the CO states are shifted to lower energy levels, and some empty states even cross the Fermi level, falling in the range from -9.0 to -5.0 eV. There is an apparent doublet below -8.0 eV, a peak with shoulder centered at ~ -7.0 eV, and 2 peaks at -6.0 and -5.0 eV, respectively (Fig. 4c, right panel). These can be attributed to charge transfer and variation of the hybridization state on C(CO). Formation of CO3-MS2 is exothermic by 0.27 eV, and the corresponding ΔG is -0.22 eV at 298 K.

One unexpected feature of CO3-MS2 is an ultra-long C–O bond of 1.48 Å with a C–O stretching frequency of 795 cm^{-1}. CO3-MS2 can be considered as an adduct of 2 adsorbed CO_2 molecules. In CO3-MS2, 1 CO_2 coordinates with Fe through C (0.14 $|e|$ charged) and uses the negatively charged O (-0.09 $|e|$) as a Lewis base site to bind the positively charged Lewis acidic C (0.22 $|e|$) of another CO_2 that binds Fe *via* negatively charged O (-0.18 $|e|$). Therefore, dissociation of CO3-MS2 by scission of the ultra-long C–O bond and ripening of the C=O bonds to form 2 adsorbed CO_2 would be rather facial. As expected, the calculated ΔE_r and ΔG_r values for the dissociation of CO3-MS2 are both 0.01 eV (CO3-TS2, Fig. 3e), leading to the formation of 2 adsorbed CO_2 (CO3-FS1, Fig. 3f). In CO3-TS2, the unusual C–O bond is further distorted to 1.58 Å, while the Fe–C and Fe–O distances increase to 2.01 and 1.94 Å, respectively, showing the tendency for scission of the C–O bond and weakening of the Fe–C and Fe–O interactions to form $2CO_2$. In CO3-FS1, the CO_2 formed from CO is interacting with Fe at an O–Fe distance of 2.13 Å and an Fe–O–C angle of 178.7°; meanwhile, the CO_2 originating from CO_3 is nearly in plane with the other CO_2, vertical to the graphene plane at a Fe–O distance of 3.50 Å. The charges on the C and 3O atoms of the CO_3 moiety as well as the O and C atoms of CO change to 0.23, -0.21, -0.18, -0.10, -0.16 and 0.16 $|e|$, respectively, from 0.22, -0.23, -0.18, -0.09, -0.16 and 0.15 $|e|$, respectively, in CO3-MS2, and they change further to 0.31, -0.10, -0.09, -0.08, -0.10, 0.32 $|e|$, respectively, in CO3-FS1; this indicates that Fe is being reduced while the C atoms transfer charge to O atoms and become oxidized in this process.

It should be noted that ΔG for CO3-MS1 formation and further evolution are more significant compared with that for the dissociation of C_2O_4. Due to the heterogeneous nature, the calculated ΔG for CO3-MS1 formation depends strongly on P_{CO} and temperature; however, this correlation for ΔG_r at CO3-TS1 is negligible (Fig. 3m, insets). In this sense, low temperature and a reasonable P_{CO} are favored for CO adsorption and may promote the population of CO3-MS1 as a surface species for further evolution through CO3-TS1 to CO3-FS1.

The evolution of LH-MS2 on FeGR with CO as an ancillary ligand was also investigated. Compared with the direct thermo-driven decomposition of LH-MS2 with ΔE_r and ΔG_r values of 0.75 and 0.68 eV, respectively, the calculated ΔE_r and ΔG_r values are 0.79 and 0.72 eV, respectively. In the corresponding transition state (CO3-TS3), the CO_3 moiety is significantly distorted, with extended C–O and O–Fe distances of 1.90 and 2.48 Å, respectively, and a deformed O–C–O angle of 151.5°, clearly showing the tendency for dissociation of CO_3 and detachment of a CO_2 molecule. Following CO3-TS3, the distorted CO_2 part moves far from the remnant O and ripens to form a CO_2, leaving a CO coadsorbed with the remnant O atom at the Fe center (CO3-MS3). The ΔE and ΔG values between CO3-MS2 and

CO3-MS3 are 0.24 and 0.09 eV, respectively, and the instability of CO3-MS3 can be attributed to the high reactivity of the adsorbed CO and O. The subsequent reactions would proceed with desorption of CO_2 (CO3-MS4, Fig. 3i) and the combination of coadsorbed CO and remnant O by passing a transition state with ΔE_r and ΔG_r of 0.12 and 0.06 eV, respectively, at 298 K (CO3-TS5, Fig. 3j), forming another CO_2 (CO3-FS2, Fig. 3k). Considering the rather high ΔE_r and ΔG_r with CO as an ancillary ligand, the contribution of the reactions along this pathway to the reaction kinetics would be similar to that of the direct thermo-driven dissociation of LH-MS2. The potential adsorption of O_2 at LH-MS2 was also investigated. However, the small E_{ad} (−0.02 eV), positive ΔG for O_2 adsorption (0.60 eV) and long O(O_2)–Fe distance (3.88 Å) suggest that coadsorbed O_2 may not impact the further evolution of CO_3 species. Therefore, we did not consider the reaction pathways initiated with CO3-MS5 (Fig. 3l and m) further.

From the above analysis of various potential reaction pathways and reported experimental findings, CO oxidation over FeGR would initiate with the formation of coadsorption of CO with preadsorbed O_2 and proceed through formation and dissociation of peroxide species along the conventional revised Langmuir–Hinshelwood pathway, leading to LH-FS1 (Fig. 2f). High reaction temperature promotes both peroxide dissociation and CO_2 desorption, leading to LH-FS1a (Fig. 2g and m), in which the Fe center can either be reduced with gaseous CO or react with CO_2 to form CO_3 (Fig. 2l). According to the reaction thermodynamics, formation of CO_3 species is inevitable in CO oxidation conditions and would compete with CO_2 desorption and subsequent reduction of the Fe center, especially in conditions with low temperatures and high P_{CO_2} (Fig. 2m). Furthermore, CO adsorption and incorporation into CO_3 species was proposed in this work for the evolution of CO_3 species on FeGR and is plausible, involving the formation and dissociation of C_2O_4 to adsorbed CO_2. Although this pathway is reaction condition-dependent (Fig. 3m), it will, at least, act as a supplement to the conventional revised Langmuir–Hinshelwood pathway that is the dominant pathway at high temperatures for CO oxidation over SACs, and it will contribute positively to CO conversion, especially at low temperatures.

4. Conclusions

We extended the CO oxidation reaction network on FeGR by extensive first-principles-based calculations. FeGR-catalyzed CO oxidation initiates with a conventional revised Langmuir–Hinshelwood pathway through CO-assisted scission of the O–O bond in peroxide species. We propose that CO_3 forms from CO_2 and NCSOS, even on SACs. This pathway competes with the desorption of CO_2 and the reduction of the Fe center with gaseous CO, and it is exothermic and inevitable, especially at low temperatures and with high P_{CO_2}. Although direct dissociation of CO_3 is demanding, further adsorption of CO on Fe in CO_3 is plausible and takes place spontaneously. A new pathway for the evolution of CO_3 involving a reaction between adsorbed CO and CO_3, forming a cyclic-carbonate-like species that dissociates easily to CO_2, was proposed. This newly proposed pathway for CO_3 evolution would compete with the conventional revised Langmuir–Hinshelwood pathway and contribute positively to CO conversion, especially at low temperatures. These findings highlight the reaction condition-dependent formation and evolution of carbonate species as well as its contribution to CO conversion, and it may extend the understanding of the catalytic performance of SACs in low temperature CO oxidation. Further investigations on the reaction kinetics and factors that may promote the evolution of carbonate species would be vital to improve the performance of existing SACs and for the design of new ones with superior performance for CO oxidation.

Author contributions

X. L. conceived the research and wrote the manuscript. Z. J. and X. N. F. performed the calculations and analyzed the results with the help of X. Z., Y. W., H. Z., Y. Y. and Y. S. X. N. F. and Z. J. are responsible for all the results disclosed. X. L., Y. H. and C. M. provided the materials and tools, commented the results and the manuscript. X. L. and X. N. F. finalized the manuscript. All authors have given approval to the final version of the manuscript.

Conflicts of interest

There are no conflicts to declare.

Acknowledgements

This work was supported by NSFC (21771029, 11811530631, 21573034, 21373036, 21103015 and 21771030). X. L. would also acknowledge the support the Special Academic Partner GCR Program from King Abdullah University of Science and Technology (KAUST). The supercomputer time was supported by the High Performance Computing Center at Dalian University of Technology and Supercomputing Core Lab at KAUST.

References

1 B. Meunier, S. P. de Visser and S. Shaik, *Chem. Rev.*, 2004, **104**, 3947–3980.
2 S. Kille, F. E. Zilly, J. P. Acevedo and M. T. Reetz, *Nat. Chem.*, 2011, **3**, 738–743.
3 B. K. Burgess and D. J. Lowe, *Chem. Rev.*, 1996, **96**, 2983–3011.
4 E. A. Ambundo, R. A. Friesner and S. J. Lippard, *J. Am. Chem. Soc.*, 2002, **124**, 8770–8771.
5 B. Ensing, F. Buda, M. C. M. Gribnau and E. J. Baerends, *J. Am. Chem. Soc.*, 2004, **126**, 4355–4365.
6 T. K. Das, M. Couture, Y. Ouellet, M. Guertin and D. L. Rousseau, *Proc. Natl. Acad. Sci. U. S. A.*, 2001, **98**, 479–484.
7 E. V. Kudrik, P. Afanasiev, L. X. Alvarez, P. Dubourdeaux, M. Clemancey, J. M. Latour, G. Blondin, D. Bouchu, F. Albrieux, S. E. Nefedov and A. B. Sorokin, *Nat. Chem.*, 2012, **4**, 1024–1029.

8 D. Deng, X. Chen, L. Yu, X. Wu, Q. Liu, Y. Liu, H. Yang, H. Tian, Y. Hu, P. Du, R. Si, J. Wang, X. Cui, H. Li, J. Xiao, T. Xu, J. Deng, F. Yang, P. N. Duchesne, P. Zhang, J. Zhou, L. Sun, J. Li, X. Pan and X. Bao, *Sci. Adv.*, 2015, **1**, 1500462.
9 X. Li, C.-S. Cao, S.-F. Hung, Y.-R. Lu, W. Cai, A. I. Rykov, S. Miao, S. Xi, H. Yang, Z. Hu, J. Wang, J. Zhao, E. E. Alp, W. Xu, T.-S. Chan, H. Chen, Q. Xiong, H. Xiao, Y. Huang, J. Li, T. Zhang and B. Liu, *Chem*, 2020, **6**, 3440–3454.
10 J. Y. Liu, *ACS Catal.*, 2017, **7**, 34–59.
11 X. F. Yang, A. Q. Wang, B. T. Qiao, J. Li, J. Y. Liu and T. Zhang, *Acc. Chem. Res.*, 2013, **46**, 1740–1748.
12 M. B. Gawande, P. Fornasiero and R. Zbořil, *ACS Catal.*, 2020, **10**, 2231–2259.
13 S. P. Ding, M. J. Hulsey, J. Perez-Ramirez and N. Yang, *Joule*, 2019, **3**, 2897–2929.
14 L. C. Liu, D. M. Meira, R. Arenal, P. Concepcion, A. V. Puga and A. Corma, *ACS Catal.*, 2019, **9**, 10626–10639.
15 A. Q. Wang, J. Li and T. Zhang, *Nat. Rev. Chem.*, 2018, **2**, 65–81.
16 X. Liu, C. Meng and Y. Han, *Phys. Chem. Chem. Phys.*, 2012, **14**, 15036–15045.
17 X. Chen, L. Yu, S. Wang, D. Deng and X. Bao, *Nano Energy*, 2017, **32**, 353–358.
18 X. Cui, P. Ren, D. Deng, J. Deng and X. Bao, *Energy Environ. Sci.*, 2016, **9**, 123–129.
19 A. Zitolo, V. Goellner, V. Armel, M. T. Sougrati, T. Mineva, L. Stievano, E. Fonda and F. Jaouen, *Nat. Mater.*, 2015, **14**, 937–942.
20 H. T. Chung, D. A. Cullen, D. Higgins, B. T. Sneed, E. F. Holby, K. L. More and P. Zelenay, *Science*, 2017, **357**, 479–483.
21 L. Huang, J. X. Chen, L. F. Gan, J. Wang and S. J. Dong, *Sci. Adv.*, 2019, **5**, aav5490.
22 H. Guo, M. Li, X. Liu, C. Meng, R. Linguerri, Y. Han and G. Chambaud, *Catal. Sci. Technol.*, 2017, **7**, 2012–2021.
23 Y. F. Li, Z. Zhou, G. T. Yu, W. Chen and Z. F. Chen, *J. Phys. Chem. C*, 2010, **114**, 6250–6254.
24 T. Kropp and M. Mavrikakis, *ACS Catal.*, 2019, **9**, 6864–6868.
25 X. J. Cui, H. B. Li, Y. Wang, Y. L. Hu, L. Hua, H. Y. Li, X. W. Han, Q. F. Liu, F. Yang, L. M. He, X. Q. Chen, Q. Y. Li, J. P. Xiao, D. H. Deng and X. H. Bao, *Chem*, 2018, **4**, 1902–1910.
26 X. Guo, G. Fang, G. Li, H. Ma, H. Fan, L. Yu, C. Ma, X. Wu, D. Deng, M. Wei, D. Tan, R. Si, S. Zhang, J. Li, L. Sun, Z. Tang, X. Pan and X. Bao, *Science*, 2014, **344**, 616–619.
27 F. Y. Li, X. Y. Liu and Z. F. Chen, *Small Methods*, 2019, **3**, 9.
28 F. Y. Li, J. J. Zhao and Z. F. Chen, *J. Phys. Chem. C*, 2012, **116**, 2507–2514.
29 L. Zhang, Y. Jia, G. Gao, X. Yan, N. Chen, J. Chen, M. T. Soo, B. Wood, D. Yang, A. Du and X. Yao, *Chem*, 2018, **4**, 285–297.
30 J. Q. Guan, Z. Y. Duan, F. X. Zhang, S. D. Kelly, R. Si, M. Dupuis, Q. G. Huang, J. Q. Chen, C. H. Tang and C. Li, *Nat. Catal.*, 2018, **1**, 870–877.
31 Y. Feng, L. Zhou, Q. Wan, S. Lin and H. Guo, *Chem. Sci.*, 2018, **9**, 5890–5896.
32 F. Huang, Y. Deng, Y. Chen, X. Cai, M. Peng, Z. Jia, P. Ren, D. Xiao, X. Wen, N. Wang, H. Liu and D. Ma, *J. Am. Chem. Soc.*, 2018, **140**, 13142–13146.
33 J. B. Xi, H. Y. Sung, D. Wang, Z. Y. Zhang, X. M. Duan, J. W. Xiao, F. Xiao, L. M. Liu and S. Wang, *Appl. Catal., B*, 2018, **225**, 291–297.
34 X. Liu, M. Xu, L. Wan, H. Zhu, K. Yao, R. Linguerri, G. Chambaud, Y. Han and C. Meng, *ACS Catal.*, 2020, **10**, 3084–3093.
35 H. Yan, H. Cheng, H. Yi, Y. Lin, T. Yao, C. L. Wang, J. J. Li, S. Q. Wei and J. L. Lu, *J. Am. Chem. Soc.*, 2015, **137**, 10484–10487.
36 F. Huang, Y. C. Deng, Y. L. Chen, X. B. Cai, M. Peng, Z. M. Jia, P. J. Ren, D. Q. Xiao, X. D. Wen, N. Wang, H. Y. Liu and D. Ma, *J. Am. Chem. Soc.*, 2018, **140**, 13142–13146.
37 G. J. Lan, Q. F. Ye, Y. N. Zhu, H. D. Tang, W. F. Han and Y. Li, *ACS Appl. Nano Mater.*, 2020, **3**, 3004–3010.
38 R. H. Lin, D. Albani, E. Fako, S. K. Kaiser, O. V. Safonova, N. Lopez and J. Perez-Ramirez, *Angew. Chem., Int. Ed.*, 2019, **58**, 504–509.
39 X. Liu, Y. Yang, M. Chu, T. Duan, C. Meng and Y. Han, *Catal. Sci. Technol.*, 2016, **6**, 1632–1641.
40 Y. H. Lu, M. Zhou, C. Zhang and Y. P. Feng, *J. Phys. Chem. C*, 2009, **113**, 20156–20160.
41 J. Zhang, Y. Deng, X. Cai, Y. Chen, M. Peng, Z. Jia, Z. Jiang, P. Ren, S. Yao, J. Xie, D. Xiao, X. Wen, N. Wang, H. Liu and D. Ma, *ACS Catal.*, 2019, **9**, 5998–6005.
42 X. Liu, Y. Sui, T. Duan, C. Meng and Y. Han, *Phys. Chem. Chem. Phys.*, 2014, **16**, 23584–23593.
43 S. H. Sun, G. X. Zhang, N. Gauquelin, N. Chen, J. G. Zhou, S. L. Yang, W. F. Chen, X. B. Meng, D. S. Geng, M. N. Banis, R. Y. Li, S. Y. Ye, S. Knights, G. A. Botton, T. K. Sham and X. L. Sun, *Sci. Rep.*, 2013, **3**, 9.
44 C. H. Zhang, J. W. Sha, H. L. Fei, M. J. Liu, S. Yazdi, J. B. Zhang, Q. F. Zhong, X. L. Zou, N. Q. Zhao, H. S. Yu, Z. Jiang, E. Ringe, B. I. Yakobson, J. C. Dong, D. L. Chen and J. M. Tour, *ACS Nano*, 2017, **11**, 6930–6941.
45 H. Y. Zhuo, X. Zhang, J. X. Liang, Q. Yu, H. Xiao and J. Li, *Chem. Rev.*, 2020, **120**, 12315–12341.
46 X. Liu, C. Meng and Y. Han, *J. Mol. Eng. Mater.*, 2015, **3**, 1540002.
47 M. Z. Jian, C. L. Zhao and W. X. Li, *ChemPhysChem*, 2020, **21**, 2417–2425.
48 S. Q. Peng, X. S. Lin, X. G. Song, Y. Liu, Z. Jiang, P. Hemberger, A. Bodi and Y. J. Ding, *J. Catal.*, 2020, **381**, 193–203.
49 C. Dessal, T. Len, F. Morfin, J. L. Rousset, M. Aouine, P. Afanasiev and L. Piccolo, *ACS Catal.*, 2019, **9**, 5752–5759.
50 L. Piccolo, *Catal. Today*, 2020, DOI: 10.1016/j.cattod.2020.03.052.
51 X. Liu, M. Xu, Y. Han and C. Meng, *Phys. Chem. Chem. Phys.*, 2020, **22**, 25841–25847.
52 A. D. Allian, K. Takanabe, K. L. Fujdala, X. Hao, T. J. Truex, J. Cai, C. Buda, M. Neurock and E. Iglesia, *J. Am. Chem. Soc.*, 2011, **133**, 4498–4517.
53 S. Lin, X. Ye, R. S. Johnson and H. Guo, *J. Phys. Chem. C*, 2013, **117**, 17319–17326.
54 K. K. Mao, L. Li, W. H. Zhang, Y. Pei, X. C. Zeng, X. J. Wu and J. L. Yang, *Sci. Rep.*, 2014, **4**, 5441.

55 X. Liu, Y. Sui, T. Duan, C. Meng and Y. Han, *Catal. Sci. Technol.*, 2015, **5**, 1658–1667.
56 K. Ding, A. Gulec, A. M. Johnson, N. M. Schweitzer, G. D. Stucky, L. D. Marks and P. C. Stair, *Science*, 2015, **350**, 189–192.
57 M. A. Newton, D. Ferri, G. Smolentsev, V. Marchionni and M. Nachtegaal, *Nat. Commun.*, 2015, **6**, 9675.
58 M. A. Newton, D. Ferri, G. Smolentsev, V. Marchionni and M. Nachtegaal, *J. Am. Chem. Soc.*, 2016, **138**, 13930–13940.
59 B. Delley, *J. Chem. Phys.*, 1990, **92**, 508–517.
60 B. Delley, *J. Chem. Phys.*, 2000, **113**, 7756–7764.
61 J. P. Perdew, K. Burke and M. Ernzerhof, *Phys. Rev. Lett.*, 1996, **77**, 3865–3868.
62 B. Delley, *Phys. Rev. B: Condens. Matter Mater. Phys.*, 2002, **66**, 155125.
63 D. Rappoport, N. R. M. Crawford, F. Furche and K. Burke, *Encyclopedia of Inorganic Chemistry*, John Wiley & Sons, Ltd, 2006, pp. 1–14, DOI: 10.1002/0470862106.ia615.
64 Y. Inada and H. Orita, *J. Comput. Chem.*, 2008, **29**, 225–232.
65 N. Govind, M. Petersen, G. Fitzgerald, D. King-Smith and J. Andzelm, *Comput. Mater. Sci.*, 2003, **28**, 250–258.
66 H. J. Monkhorst and J. D. Pack, *Phys. Rev. B: Solid State*, 1976, **13**, 5188–5192.
67 F. L. Hirshfeld, *Theor. Chim. Acta*, 1977, **44**, 129–138.
68 A. H. Castro Neto, F. Guinea, N. M. R. Peres, K. S. Novoselov and A. K. Geim, *Rev. Mod. Phys.*, 2009, **81**, 109–162.
69 C. D. Versteylen, N. H. van Dijk and M. H. F. Sluiter, *Phys. Rev. B*, 2017, **96**, 13.
70 Y. C. Ma, P. O. Lehtinen, A. S. Foster and R. M. Nieminen, *New J. Phys.*, 2004, **6**, 68.
71 A. V. Krasheninnikov, P. O. Lehtinen, A. S. Foster, P. Pyykko and R. M. Nieminen, *Phys. Rev. Lett.*, 2009, **102**, 126807.
72 X. Y. Xu, H. Y. Xu, H. S. Guo and C. Y. Zhao, *Appl. Surf. Sci.*, 2020, **523**, 9.
73 M. J. Kale and P. Christopher, *ACS Catal.*, 2016, **6**, 5599–5609.
74 W. F. Edgell, W. E. Wilson and R. Summitt, *Spectrochim. Acta*, 1963, **19**, 863–872.
75 M. O. Ozbek and J. W. Niemantsverdriet, *J. Catal.*, 2014, **317**, 158–166.
76 T. Li, X. D. Wen, Y. W. Li and H. J. Jiao, *Surf. Sci.*, 2019, **689**, 8.
77 X. H. Yu, X. M. Zhang, L. X. Jin and G. Feng, *Phys. Chem. Chem. Phys.*, 2017, **19**, 17287–17299.
78 M. Moses-DeBusk, M. Yoon, L. F. Allard, D. R. Mullins, Z. Wu, X. Yang, G. Veith, G. M. Stocks and C. K. Narula, *J. Am. Chem. Soc.*, 2013, **135**, 12634–12645.
79 C. Q. Ma, B. P. Liu and S. H. Yan, *Mol. Catal.*, 2020, **495**, 111165.
80 X. Zhang, Z. Lu, G. Xu, T. Wang, D. Ma, Z. Yang and L. Yang, *Phys. Chem. Chem. Phys.*, 2015, **17**, 20006–20013.
81 X. Liu, T. Duan, Y. Sui, C. Meng and Y. Han, *RSC Adv.*, 2014, **4**, 38750–38760.
82 S. C. Ammal and A. Heyden, *ACS Catal.*, 2017, **7**, 301–309.
83 K. R. Kopecky and R. R. Gomez, *Can. J. Chem.*, 1984, **62**, 277–279.
84 C. K. Narula, L. F. Allard and Z. L. Wu, *Sci. Rep.*, 2017 **7**, 8.
85 X. Liu, Y. Sui, C. Meng and Y. Han, *RSC Adv.*, 2014, **4**, 22230–22240.
86 A. Krasheninnikov, P. Lehtinen, A. Foster, P. Pyykkö and R. Nieminen, *Phys. Rev. Lett.*, 2009, **102**, 126807.
87 Y. Tang, J. Zhou, Z. Shen, W. Chen, C. Li and X. Dai, *RSC Adv.*, 2016, **6**, 93985–93996.
88 Y. Zhao, X. Liu, K. X. Yao, L. Zhao and Y. Han, *Chem. Mater.*, 2012, **24**, 4725–4734.
89 B. T. Qiao, A. Q. Wang, X. F. Yang, L. F. Allard, Z. Jiang, Y. T. Cui, J. Y. Liu, J. Li and T. Zhang, *Nat. Chem.*, 2011, **3**, 634–641.
90 H. Y. Wang and W. F. Schneider, *Phys. Chem. Chem. Phys.*, 2010, **12**, 6367–6374.